PCCP

Accepted Manuscript

ROYAL SOCIETY OF CHEMISTRY

www.rsc.org/pccp

Carbon monoxide oxidation catalysed by defective palladium chloride: DFT calculations, EXAFS, and *in situ* DRIRS measurements

Qiaohong Li[a], Luyang Qiao[a], Ruiping Chen[a], Zuju Ma[a], Rui Si[b], Yuangen Yao[a]*, Kechen Wu[a]*[1]

[a]*Key Laboratory of Coal to Ethylene Glycol and Its Related Technology, Fujian Institute of Research on the Structure of Matter, Chinese Academy of Sciences, Fuzhou 350002, PR China*

[b]*Shanghai Institute of Applied Physics, Chinese Academy of Sciences, Shanghai Synchrotron Radiation Facility, Shanghai 201204, PR China*

ABSTRACT

We examined the potential catalytic role of the palladium chloride catalyst in CO oxidation using density functional theory and experimental investigations. The active plane of the palladium chloride catalyst is identified as (140). We found that the defective $PdCl_2$ (140) surface is able to facilitate the activation of O_2 and subsequently promote the oxidation of CO. The most significant reaction channel, the Eley-Rideal mechanism (M_{ER1}), proceeds first by a peroxo-type (OOCO) intermediate formation, second by O adsorption with the first CO_2 release, then by the second CO attraction and the second CO_2 formation, and finally by the second CO_2 desorption and restoration of the defective $PdCl_2$ (140) surface. The rate-determining step is the formation of the second CO_2 in the whole catalytic cycle. Compared to the previously reported catalytic systems, the reaction activation barrier (0.54 eV) of CO oxidation in the $PdCl_2$ catalyst is low, indicating as a potential high-performance catalyst for CO

[1] Corresponding author. Fax: +86 591 83792932.
E-mail address:wkc@fjirsm.ac.cn(K. Wu).

oxidation. The present results enrich our understanding of CO oxidation of Pd-based catalysts and provide a basis for fabricating Pd-based catalysts with high activity.

Keywords: carbon oxide, palladium chloride, defective $PdCl_2$ (140) surface, CO oxidation mechanism, Pd-based catalyst

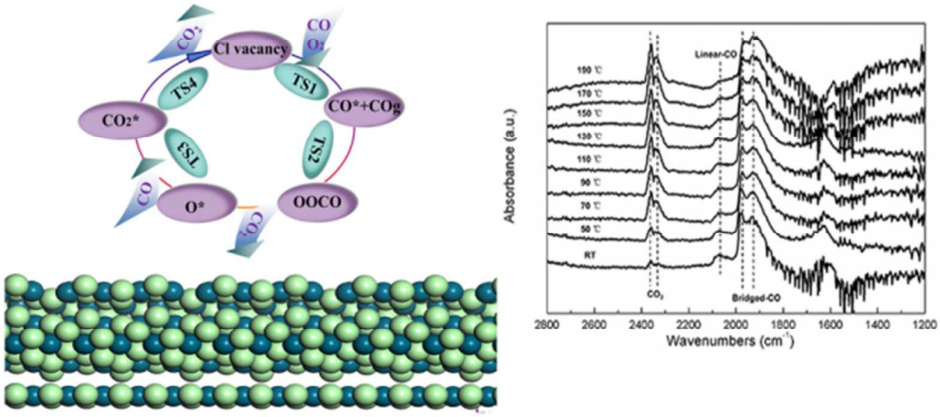

The defective palladium chloride catalysts indicate as a potential high-performance catalyst for carbon monoxide oxidation.

1. Introduction

For decades, CO has attracted particular interest and been extensively investigated both because of the abatement of toxic pollutant CO and because of its many practical applications, such as developing CO sensors and CO_2 lasers[1-10]. A significant number of noble metals[9, 11-16], such as Pt, Au, Ir, Pd, Cu, metal oxides[6, 7, 17], and doped oxides[11, 12, 18-21], have been identified as active catalysts for CO oxidation. One of the significant goals of this study was to explore the relationship between the catalytic behaviour and the electronic structure of the active sites.

Pd-based catalysts have been found to be excellent candidates for CO oxidation.[21-25] Peterson and co-workers[21] studied low-temperature CO oxidation catalysed by re-generable, atomically dispersed palladium on alumina, and their results suggested that isolated palladium atoms can be catalytically active on industrially relevant alumina γ-supports by aberration-corrected scanning transmission electron microscopy (STEM). Uchiumi *et al*[26] have reviewed oxidative reactions from carbon monoxide by a palladium-alkyl nitrite system. Kalita and Deka[23] have reported the reaction intermediates of CO oxidation on gas phase Pd_4 clusters and have found that Pd_4^0 and Pd_4^+ clusters are more suitable catalysts compared to Pd_4^- clusters. Pd-Au bimetallic catalysts for the CO oxidation reaction have been studied using DFT calculations, which have predicted that the [Pd](Au) core/shell nanoparticle catalyst should have a higher activity toward CO oxidation because it combines the advantages of the ligand effect of Au and the strain effect of Pd.[25] Our group designed Pd doped on an

α-Al_2O_3(0001) surface with a Pd_3O_9 cluster and investigated the CO oxidation mechanism using DFT, and our results implied that the Pd_3O_9@ Al_2O_3 catalyst showed superior catalytic activity toward CO oxidation. However, so far, little has been reported with regard to the $PdCl_2$ surface.

Wang *et al*[27] reported that $PdCl_2$-$CuCl_2$-KOAc/AC@Al_2O_3 is highly efficient for gas-phase oxidative carbonylation of methanol to dimethyl carbonate and further proposed the catalytic reaction mechanism. The $PdCl_2$ catalyst has been determined, using indirect methods, to be effective in the synthesis of dimethyl carbonate (DMC) in experiments;[28] however, its catalytic activity decreased with the passage of time, as determined by the loss of Cl^-. Recently, Wang's group[29] studied the surface structure and reaction properties of the $CuCl_2$-$PdCl_2$ bimetallic catalyst in the oxycarbonylation of methanol with DFT. On the $CuCl_2$-$PdCl_2$ surface, the active site for methanol oxidation was determined to be Cu-Cl-Cu (Pd). However, very little is known about the detailed structural information of adsorbed CO and the CO oxidative mechanism on the $PdCl_2$ surface. Considering the importance of palladium-based catalysts in CO oxidation, the study herein focuses on the detailed reaction mechanism of CO oxidation over a defective $PdCl_2$ (140) surface. In this study, we have examined the reaction pathway of CO oxidation through DFT computations and through high-resolution transmission electron microscopy (HRTEM), X-ray photoelectron spectroscopy (XPS), extended X-ray absorption fine structure (EXAFS) spectra, X-ray absorption near-edge structure (XANES) spectra, and *in situ* DRIRS measurements. To

elucidate the nature of the binding of the $PdCl_2$ catalyst surface and the mechanism of CO oxidation on this catalyst, the possible catalytic reaction pathways of CO oxidation on the defective $PdCl_2$ (140) surface and the electronic properties of the reactant, transition state (TS), and intermediate product have been simulated. Mulliken charge analysis and the relative density of states (DOS) were also calculated to evaluate the performance of the $PdCl_2$ catalyst for CO oxidation. On the basis of these experimental and theoretical results, we expect to provide a better understanding of CO oxidation on Pd-based catalysts and bring forward a basis for fabricating Pd-based catalysts with high activity.

2. Experimental

2.1 DFT

As an inert carrier, the effect of α-Al_2O_3 was not considered in this study. The $PdCl_2$ (140) perfect surface is represented by seven-layer slabs (the Cl-Pd-Cl chain denotes one layer) with a (2×2) supercell, as shown in Fig. 1. $PdCl_2$ is composed of a chain structure of Pd connected by doubly coordinated Cl, whereas the interchain interaction occurs primarily via van der Walls. Without the adsorbate, the vacuum between the slabs is set to span a range of 15 Å. All of the atoms of the two bottom layers were fixed to the bulk positions. The adsorbate was set on one side of the slab. The calculation details were tested to be sufficient to yield accurate results.

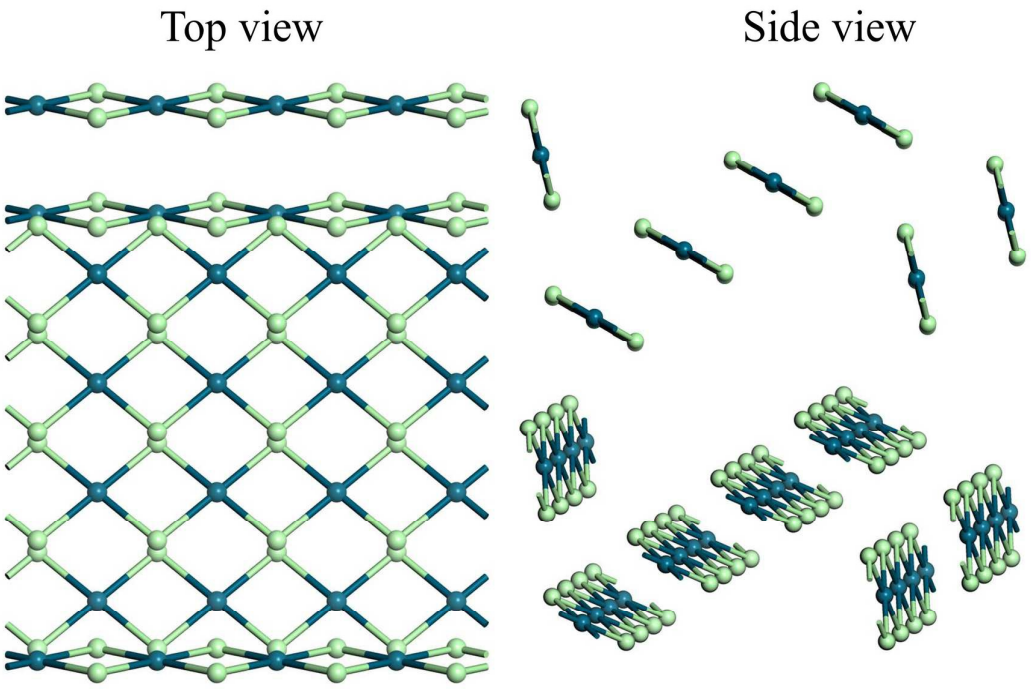

Fig. 1. Top and side views of the perfect $PdCl_2$ (140) surface. The Pd and Cl atoms are coloured in blue and green, respectively.

All of the calculations were performed within the density functional theory (DFT) approach using the Dmol^3 software package,[30, 31] which can simulate periodic systems. The generalized gradient approximation (GGA) is adopted to describe the density functional using the Perdew and Wang (PW91)[32] functional for the exchange-correlation term. The wave functions were expanded in terms of numerical basis sets. The double-numeric quality basis set with polarization functions (DNP[30, 33, 34]) was adopted, which is comparable to 6-31G**[35-37]. The numerical basis sets can minimize the basis set superposition error[38]. All-electron basis sets were used for all of the elements except Pd, which was treated by using the effective core potential. A Fermi smearing of 0.005 hartree was utilized and a Monkhorst-Pack *k*-point grid of size of 3×3×1 was used for structural relaxation and TSs location. The energy tolerance, gradient, and displacement convergence

were 1×10^{-5} hartree, 2×10^{-3} hartree/Å, and 5×10^{-3} Å, respectively. The transition states were located using the complete linear synchronous transit/quadratic synchronous transit (LST/QST) methods. The reliability of the method has been confirmed by previous reports of studies on the mechanism of DMC (dimethyl carbonate), DMO (dimethyl oxalate) and CO_2 synthesis[5, 17, 39-44].

The adsorption energies ΔE_{ads} are defined as:

$$\Delta E_{ads} = E_{total} - (E_{slab} + E_{adsorbate}) \qquad (1)$$

in which E_{total} represents the total energy for the slabs with adsorbate, E_{slab} represents the total energy of the bare slab of the surface, and $E_{adsorbate}$ represents the total energies of free adsorbate molecules.

2.2 Catalyst preparation and characterization

The $PdCl_2/\alpha$-Al_2O_3(2.0 wt.% Pd) catalysts were prepared by wet impregnation of $PdCl_2$ (AR, Sino-Platinum Co., Ltd., China) in diluted hydrochloric acid solution; the solution was dried at 393 K for 12 h and then reduced under an atmosphere containing 10 vol.% H_2 in Ar at 150℃ for 30 min.

The samples for the TEM and HRTEM observations were prepared by drying a drop of a diluted ethanol dispersion of the $PdCl_2/\alpha$-Al_2O_3 catalyst on copper grids. The particle sizes and shapes were examined by a transmission electron microscope (JEM-2010) operated at 200 kV, equipped with a Gatan-794-MSC CCD camera system, a Gatan-676TV system, and an OXFORD-INCA ultra-thin window EDS system.

XPS was obtained using a VG MultiLab 2000 analyser with a Mg $K\alpha$ radiation

source; the binding energies were referenced to C 1*s* (284.6 eV).

The *in situ* DRIRS measurements were performed on a Fourier transform infrared spectrometer Nicolet 6700 equipped with a stainless steel *in situ* IR flow cell. The powder samples were placed into the cell after pre-treatment under N_2 flow for 30 min at 423 K. The reference spectrum was collected when the sample cooled down to a desired temperature. Then, spectra were recorded with a resolution of 4 cm^{-1} for 64 scans after the reactants were introduced into the reaction cell at a constant flow rate.

2.3 X-ray absorption spectroscopy

The EXAFS spectra and XANES spectra of the Pd K edge were measured at the BL14W1 beamline, Shanghai Synchrotron Radiation Facility (SSRF), with an electron beam energy of 3.5 GeV under "top-up" mode (current: 220 mA). The samples were analysed at room temperature using a fixed-exit monochromator equipped with two flat Si (311) crystals. Data on the catalysts and reference samples (Pd foil and $PdCl_2$ powder) were collected in the fluorescence mode (32-element HPGe detector) or the transmission mode (Oxford ion chamber). Athena and Artemis software were used to extract the data and to fit the curves, respectively[45, 46]. The Fourier-transformed curves were fitted in real space with Δk = 2-13 $Å^{-1}$ and ΔR = 1.1-3.3 $Å^{-1}$ for Pd (k2 weighted).

2.4 Activity test and product analysis

The activities of the $PdCl_2/\alpha$-Al_2O_3 catalysts for CO oxidation were evaluated in a fixed-bed glass tubular reactor. The $PdCl_2/\alpha$-Al_2O_3 catalysts (1 g) were placed in the reactor and were purged in N_2 flow for 30 min at room temperature; then the reactant gases (CO, O_2, and N_2 balance) were passed through the reactor at a gas hourly space velocity (GHSV) of 3000 h^{-1} with a ramp rate of 2 K/min from room temperature to reaction temperature under a pressure of 0.12 MPa. The products were condensed and analysed by Agilent GC-7820A gas chromatography fitting with a flame ionization detector.

3. Results and discussion

3.1 The characterization of the catalyst

To confirm the presence of this surface in $PdCl_2/\alpha$-Al_2O_3, the sample was characterized by XPS, HRTEM, XRD, XANES, and EXAFS. The HRTEM image of the catalyst in Fig. 2A (1) shows that the interval between two lattice fringes of $PdCl_2$ NPs is approximately 0.226 nm, corresponding to the inter-planar distance of the (140) plane of $PdCl_2$[47]. The inset shows the corresponding FFT pattern of the $PdCl_2$ surface. The measured angle of 51.4° between the (140) and (211) surfaces was in agreement with the calculated data based on formula 2[48]:

$$\cos \emptyset = \frac{\frac{h_1 h_2}{a^2}+\frac{k_1 k_2}{b^2}+\frac{l_1 l_2}{c^2}}{\sqrt{(\frac{h_1^2}{a^2}+\frac{k_1^2}{b^2}+\frac{l_1^2}{c^2})(\frac{h_2^2}{a^2}+\frac{k_2^2}{b^2}+\frac{l_2^2}{c^2})}} \qquad (2)$$

in which h_1, h_2, k_1, k_2, l_1, and l_2 represent Miller indices of (140) and (211), and a, b, and c represent cell parameters.

The XRD pattern (see Fig. 2A (2)) of $PdCl_2/\alpha$-Al_2O_3 also displayed the 2θ positions of $PdCl_2$'s main peaks. The Al_2O_3 support had a diffraction pattern that was characteristic of the alpha phase[49]. The diffraction peaks at 2θ=16.7°, 40.1°, and 47° correspond to the orthorhombic $PdCl_2$ crystalline structure[48]. The sharp peaks of the catalyst may suggest the formation of a well crystalline $PdCl_2$.

According to Fig. 2A (3), on the basis of the comparative intensity of Pd peaks, we determined the ratio of $PdCl_2/Pd^0$ in the sample to be 93.8%. The result showed that the active Pd phase of the catalyst was primarily in the $PdCl_2$ state, but a small number of sites were still in the Pd^0 state. The reduction step in the catalyst preparation process induced a slight loss of chlorine and thus the defective structure of $PdCl_2$ could be identified.

The short-range structure of $PdCl_2/\alpha$-Al_2O_3 was determined from Pd K-edge XANES spectra (Fig. 2B(1)). The curve of $PdCl_2/\alpha$-Al_2O_3 fit well with the reference $PdCl_2$ powder. The Fourier-transformed k2-weighted Pd K-edge EXAFS data of the Pd particles are shown in Fig. 2B (2), (3), and Table 1. The spectra of the initial state of $PdCl_2/\alpha$-Al_2O_3 indicated that the Pd-Cl distance (R) of 2.29 Å was similar to that for pure $PdCl_2$ powder. The Pd-Cl coordination number (CN) of 5.3±0.9 for the catalyst was slightly lower than 8 for pure $PdCl_2$, suggesting that the Pd species in the catalyst were not perfect $PdCl_2$, which is in accordance with the catalyst preparation and activation process.

Both the XANES and EXAFS results clearly show that the short-range structure of Pd phases in the catalyst was in agreement with the XPS results and further

confirms the defective structure of $PdCl_2/\alpha$-Al_2O_3.

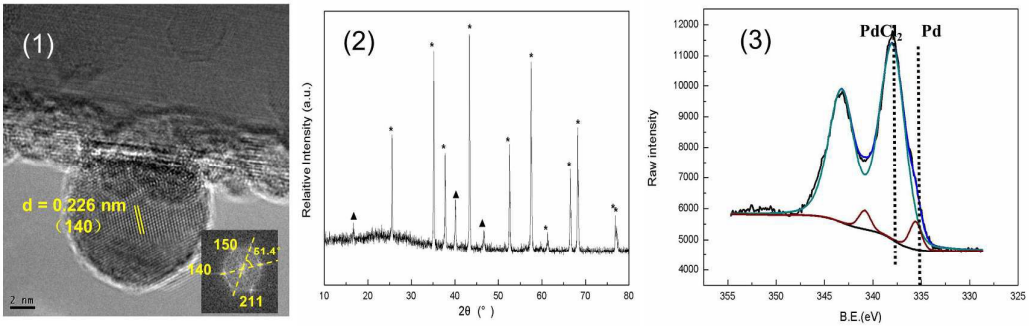

Fig. 2A. (1) HRTEM image of the fresh $PdCl_2/\alpha$-Al_2O_3 catalyst; (2) XRD profiles of the $PdCl_2/\alpha$-Al_2O_3 catalyst; (3) Curve fit of Pd and $PdCl_2$ 3d peaks for XPS profiles of the $PdCl_2/\alpha$-Al_2O_3 catalyst.

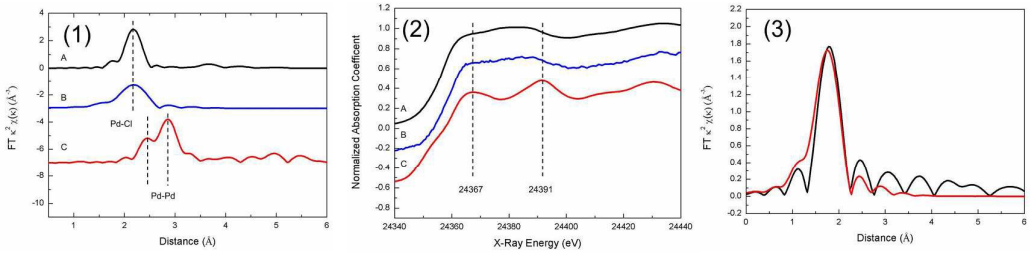

Fig. 2B. (1) XANES spectra; (2) k^2-Weighted Fourier transform Pd K-edge EXAFS spectra of the $PdCl_2/\alpha$-Al_2O_3 catalyst: (A) pure $PdCl_2$, (B) $PdCl_2/\alpha$-Al_2O_3, (C) Pd foil; (3) EXAFS data (black) and fit data (red) of the $PdCl_2/\alpha$-Al_2O_3 catalyst.

Table 1. Coordination numbers (CN), distances (R), and Debye-Waller factors for Pd-Cl and Pd-Pd bonds in the $PdCl_2/\alpha$-Al_2O_3 catalyst.

Sample	Pd-Cl		Pd-Pd		D. W.	ΔE_0 (eV)
	R (Å)	CN	R (Å)	CN		
Pd foil	–	–	2.74±0.00	12	0.006±0.000	-0.7±0.6
$PdCl_2$	2.32±0.01	8	–	–	0.006±0.001	7.4±2.2
$PdCl_2/\alpha$-Al_2O_3	2.29±0.01	5.3±0.9	–	–	0.006±0.001	0.3±1.5

3.2 Complexes of defective $PdCl_2$ (140) with CO or O_2

The reaction begins with the adsorption of CO and O_2 molecules over the defective $PdCl_2$ (140) surface, which is consistent with the experimental measurement. Considering the Cl vacancy, we tested various defect modes of

monovacancy from the defect-free $PdCl_2$ (140) surface and selected the mode that had the lowest defect forming energy. Fig. 3 displays the optimized stable geometries of individual CO or O_2 molecules after testing several defect modes. The most favourable site of single CO (M1) or O_2 (N1) molecules is bound to the chlorine vacancy (V_{Cl}), and the carbon atom (CO) or oxygen atom (O_2) approaches two Pd atoms in a bridged mode. The adsorption energy was -2.32 eV and -3.19 eV, respectively, which clearly suggests the stability of the CO and O_2 molecules on the $PdCl_2$ (140) surface. In addition, from the structural analysis, we can see that the C-O and O-O distances remarkably increased from 1.128 to 1.172 Å and from 1.207 to 1.296 Å, respectively. The C-O and O-O bonds were activated on the defective $PdCl_2$ (140) surface. Namely, O_2 exhibited a stronger interaction with the defective $PdCl_2$ (140) surface, which implies that the reaction channel where CO attacks the Pd-O_2 complex would process more favourably than the other case in which the O_2 molecule attacks the Pd-CO complex.

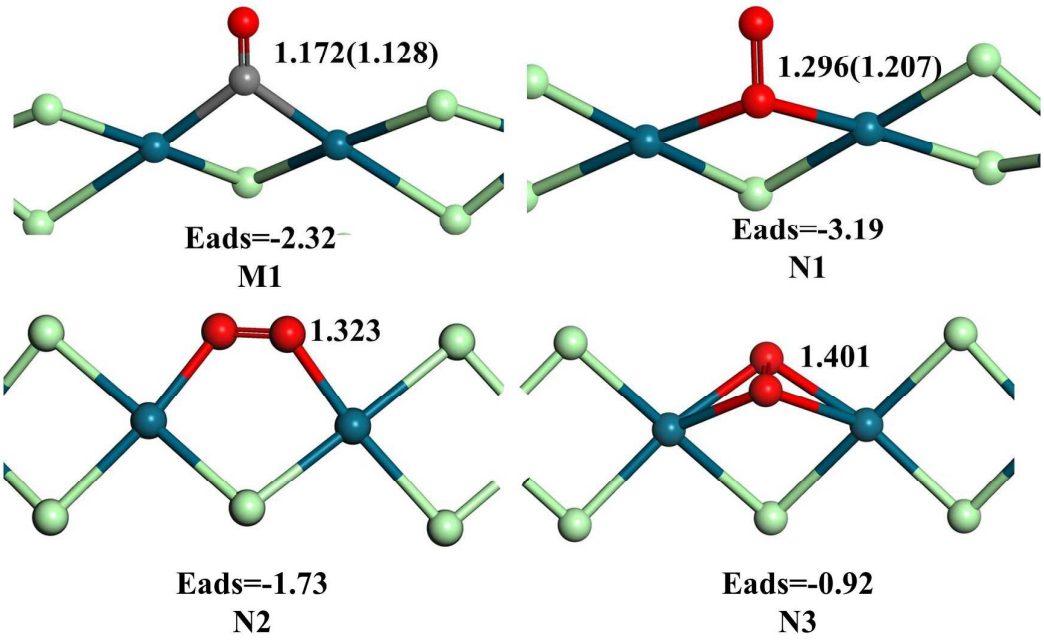

Fig. 3 Optimized stable structures of single CO (M1) and O_2 (N1-N3) molecule adsorption on a defective $PdCl_2$ (140) surface. The values in parentheses for CO and O_2 are the experimental bond lengths. The bond lengths and the adsorption energies are given in angstrom and eV, respectively. The Pd, Cl, C, and O atoms are coloured in blue, green, grey, and red, respectively. The same colour scheme is applied in Figs. 4 and 8.

3.3 Stable intermediate adsorption on defective $PdCl_2$ (140)

To map out the mechanism of the CO oxidation process, the co-adsorption of CO and O_2 molecules were studied. After testing several possible co-adsorption configurations, interestingly, we found two stable configurations that were peroxo-type (OOCO) and carbonate-like (CO_3) compounds (see Fig. 4). Compared to the individual adsorption shown in Fig. 3 for OOCO, the O-O bond was largely activated with the bond length increased from 1.296 to 1.465 Å, and the new C-O bond (1.465 Å) was formed, finally resulting in the formation of OOCO. For CO_3, the O-O bond was largely activated with the bond length increased from 1.296 to 2.249 Å, leading to breakage of the O-O bond.

Simultaneously, two new C-O bonds (1.306 and 1.346 Å) formed, ultimately bringing about the formation of CO_3. Furthermore, the adsorption energy was -4.12 and -3.81 eV, respectively. The large adsorption energy clearly suggests the stability of the OOCO and CO_3 complexes on defective $PdCl_2$ (140). Additionally, according to the atomic charges shown in Fig. 4, the C and O atoms of the newly formed C-O bond attract one another, and the electrostatic interaction further enhanced the stability of the OOCO and CO_3 intermediates, which were also observed in recent publications[5, 17].

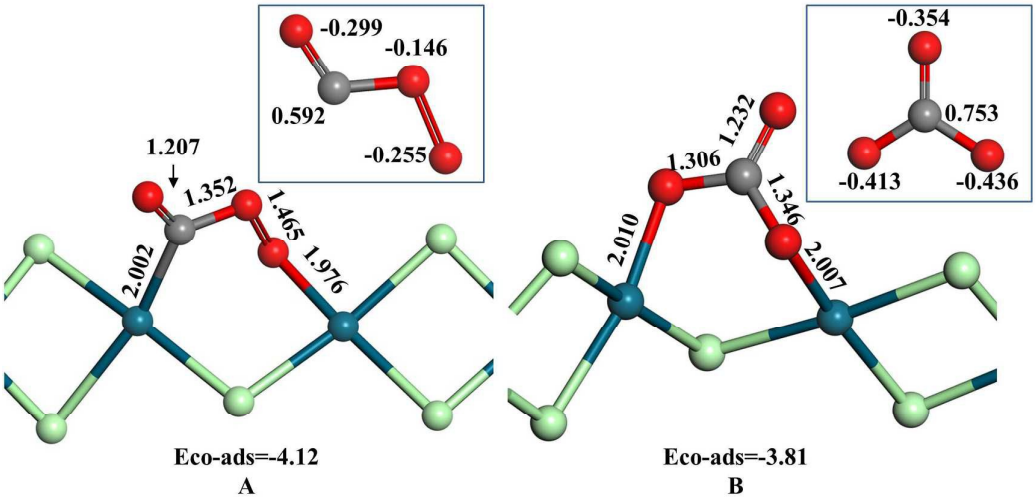

Fig. 4. Optimized stable intermediates A: peroxo-type (OOCO) and B: carbonate-like (CO_3) formed by CO and O_2 co-adsorption. The values in the blue rectangles indicate Mulliken charges. The bond lengths and the adsorption energies are given in angstrom and eV, respectively.

The DOS of the separate components (adsorbates and $PdCl_2$) in the adsorbed OOCO and CO_3 configurations is shown in Fig. 5. According to the OOCO complex (see Fig. 5(a)), the partial density of states (PDOS) plots of the interaction clearly show that a new strong C-O bond between CO and O_2 was formed, as indicated by the significant overlap between the CO and O_2 2π orbitals.

In addition, Pd 4*d*-CO 2π and Pd 4*d*-O_2 2π* interactions were observed. For the CO_3 complex (see Fig. 5(b)), there was a broadening of O_2 2π* overlap with the Pd 4*d* state, which suggests that the electrons in the Pd 4*d* orbital are transferred to the O_2 molecule, thereby leading to the rupture of the O-O bond. Simultaneously, there was good 2π overlap of CO and O_2, resulting in the formation of two new C-O bonds between CO and O_2.

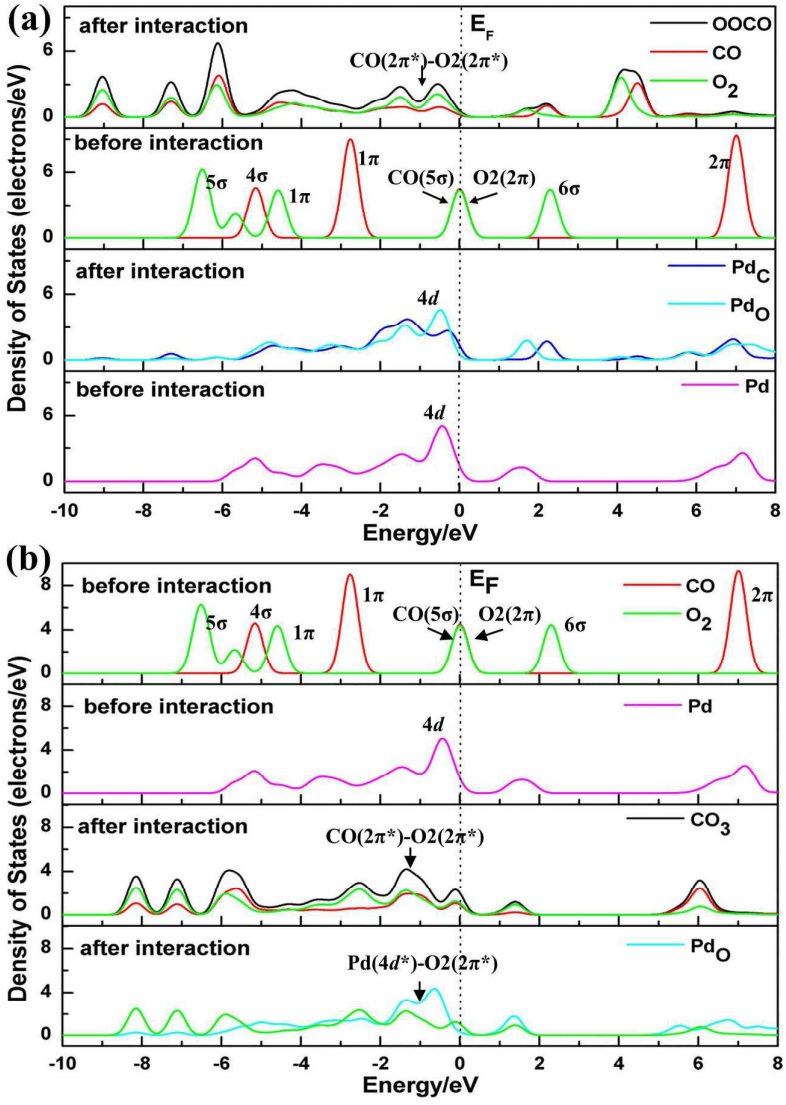

Fig. 5. DOS of the separate components (CO, O_2, and Pd, respectively) before and after adsorption. (a) for OOCO and (b) for CO_3.

3.4 *In situ* DRIR measurements

In situ infrared spectra were acquired after the reactants were injected into the reaction cell and the reaction temperature was set to the specified point. Fig. 6 shows the *in situ* DRIR spectra of the CO and O_2 reactions on the $PdCl_2$/a-Al_2O_3 catalyst at RT, 50, 70, 90, 110, 130, 150, 170, and 190 ºC. The band at approximately 2,075 cm^{-1} was assigned to linear CO, and the peaks at approximately 1,978 and 1,932 cm^{-1} were attributed to the bridge bonded CO[50]. Moreover, the peak at approximately 1,624 cm^{-1} could be assigned to the bending mode of the OH groups on the alumina surface. The bands at approximately 2,327 and 2,358 cm^{-1} [51] were attributed to the C-O stretching vibrations of the product, CO_2. All of the peaks gradually increased from RT to 190 ºC.

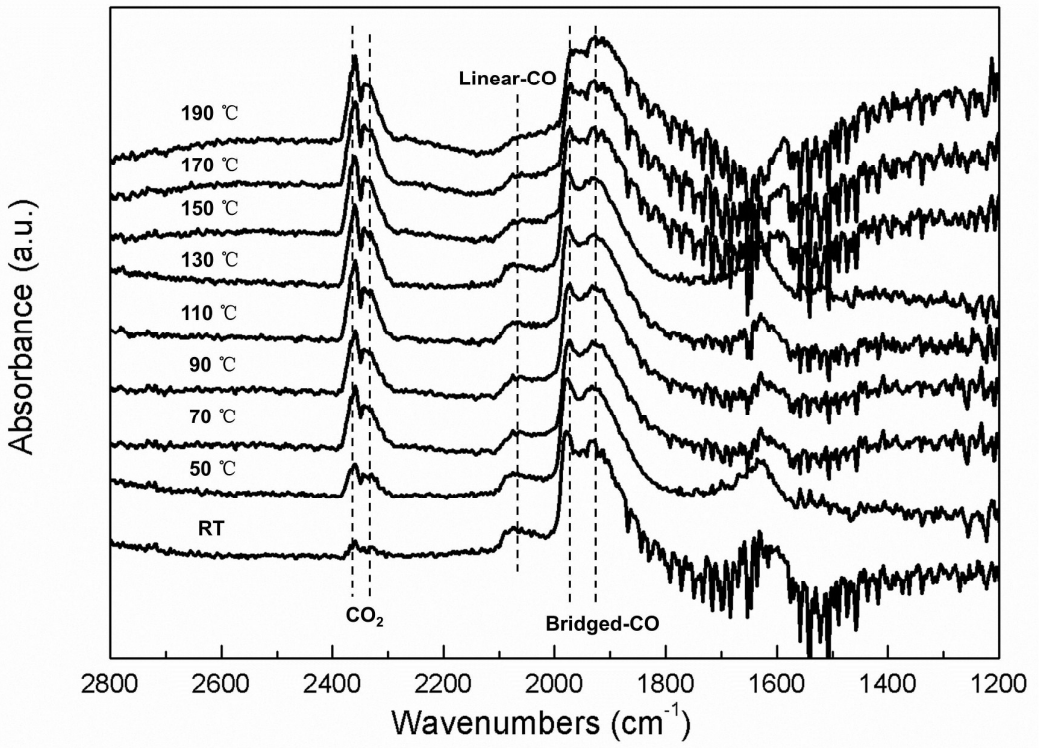

Fig. 6. IR spectra of the CO and O_2 reactions on the $PdCl_2$/α-Al_2O_3 catalyst at different temperatures. The *in situ* infrared measurements were taken through the gas, and the

temperature reached the specified temperature after balance and after 10 min data acquisition.

3.5 Reaction profiles for CO oxidation

The mechanism of the catalytic cycle of CO oxidation on the defective $PdCl_2$ (140) from the DFT calculations is depicted in Fig. 7, and the bond lengths of these structures are summarized in Fig. 8 (side view). After pre-reduction by H_2, a chlorine vacancy was formed. On the basis of the adsorption results, CO oxidation on defective $PdCl_2$ (140) was studied. Four reaction mechanisms are proposed and displayed in Fig. 7, in which the energies are also shown, and the bond lengths of these structures are summarized in Fig. 8. In these putative mechanisms, we first consider the Eley-Rideal (E-R) mechanism. The catalytic cycles are initiated by the adsorption of O_2 molecules onto the defective $PdCl_2$ (140); then, the CO gas promptly reacts with the adsorbed O_2 on the V_{Cl} site. The initial step of the reaction involves the formation of complexes in which the O_2 molecule binds to the defective $PdCl_2$(140) surface (step A).

For M_{ER1}, after overcoming an activation barrier of 0.26 eV (TS1), an intermediate (step B: peroxo-type, OOCO) is found. From the structure analysis, along the reaction coordinate, the Pd-O bond is breaking and the C-O bond is forming, resulting in the formation of an intermediate peroxo-type, OOCO (step B). Next, the cleavage of one O-O bond of OOCO occurs to produce the first CO_2 molecule and then desorbs from the surface with a low activation barrier of only 0.30 eV (TS2), which is exoergic by 2.13 eV, leaving behind an O atom bound to the defective $PdCl_2$ (140) surface (step C). The second half of the catalytic cycle

begins with the adsorbed O from the first step. The CO gas promptly reacts with the adsorbed O (step D) to reach TS3, resulting in the formation of an adsorbed CO_2 molecule (step E). The calculated activation barrier for the reaction is 0.54 eV. After passing over TS4, a CO_2 molecule is completely desorbed from the surface with an activation barrier of 0.16 eV and exothermic heat of 0.14 eV, resulting in an chlorine vacancy (V_{Cl}) (step F). Our results note that the formation of OOCO is easier than the desorption of CO_2 because the peroxo-type intermediated OOCO is very stable on the defective $PdCl_2$(140) surface. Furthermore, these values are favourable enough to make this reaction occur.

In addition to intermediate OOCO, which arose directly from adsorbed O_2 and CO gas, we also consider another intermediate, CO_3. A second possible pathway (M_{ER2}) is illustrated in Fig. 7 (blue line) and Fig. 8. Compared to M_{ER1}, however, the gaseous CO can insert into the O-O bond, via TS5, with a barrier height of 2.71 eV, forming a very stable carbonate adsorbate (step G) with an exotherm of 2.99 eV. The barrier involved in this step is so large that it is difficult to surmount. In the next desorption path from CO_3 (ads) to the product CO_2 gas (step C), a lower energy barrier of 1.61 eV (TS6) is required. It involves the scission of one O-O bond and the formation of a C-O bond, and this process is also exothermic by 0.16 eV. It is clear that although the formation of the CO_3 species (M_{ER2}) is very difficult, the significantly high barrier for CO_3 formation and dissociation on the defective $PdCl_2$ (140) surface makes the M_{ER2} path less possible for CO oxidation.

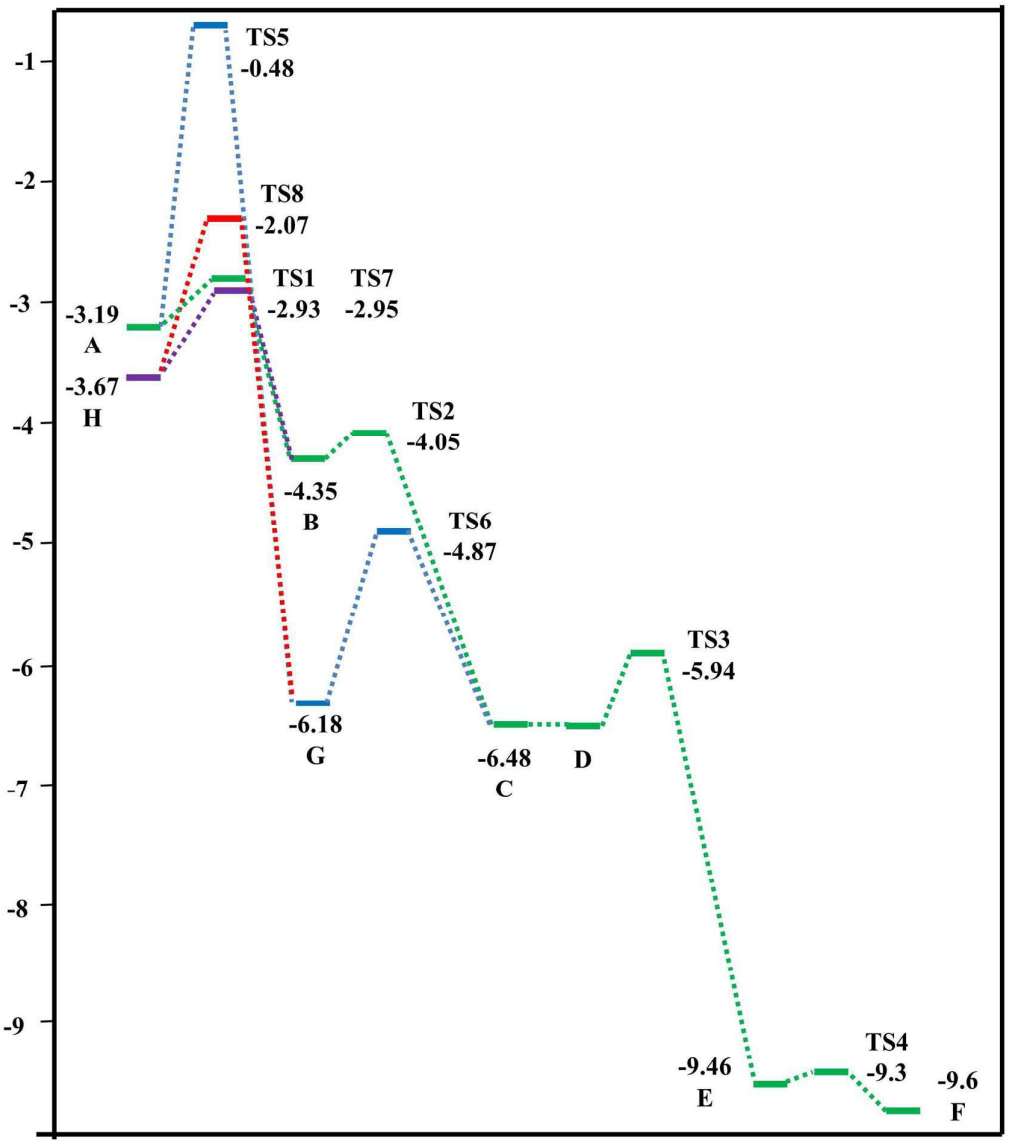

Fig. 7. Four proposed reaction pathways for CO oxidation on the defective $PdCl_2$ (140) surface. M_{ER1} (green), M_{ER2} (blue), M_{LH1} (purple), and M_{LH2} (red). The energy and bond lengths are given in eV and angstroms, respectively.

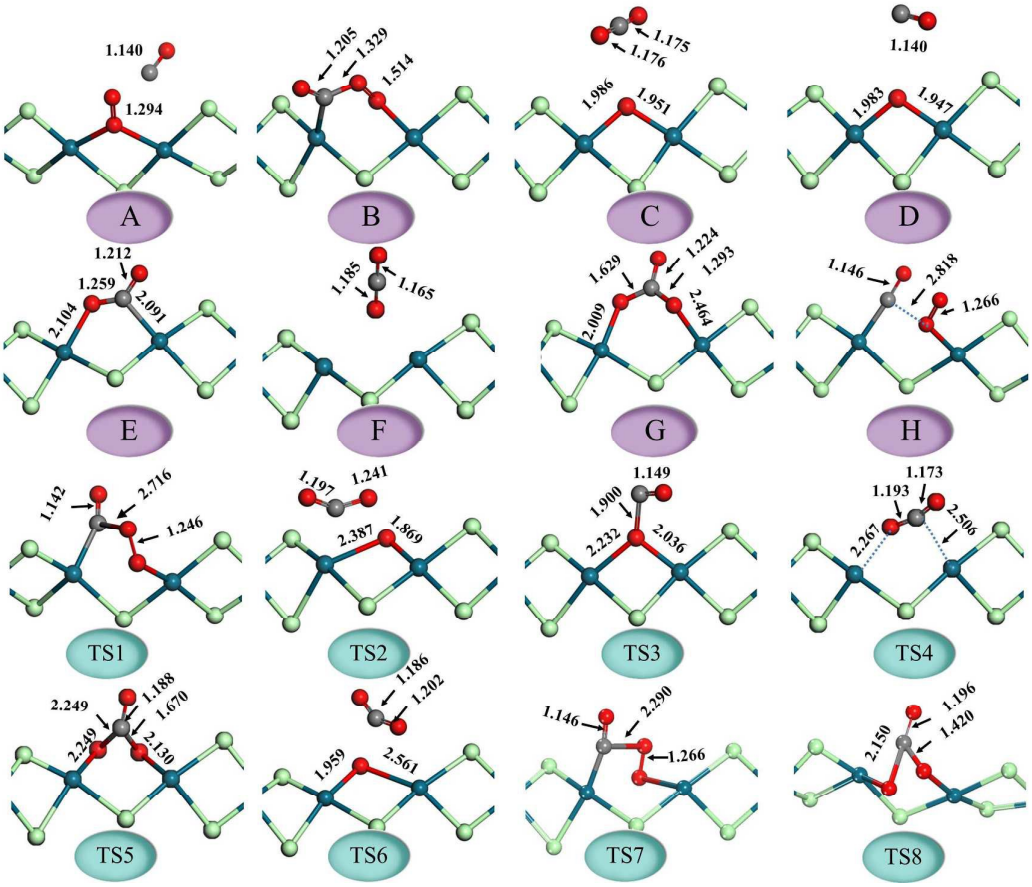

Fig. 8. Side view of the proposed reaction pathway for CO oxidation on the defective $PdCl_2$ (140) surface. See the caption of Fig. 7.

Compared to the E-R mechanism in the first half of the catalytic cycle, the Langmuir-Hinshelwood (L-H) mechanism has been calculated (see Figs. 7 and 8), in which the adsorption of O_2 on the V_{Cl} site is competing with adsorbed CO. The co-adsorption energy of two adsorbed CO molecules and one adsorbed O_2 molecule (step H) is -3.67 eV, which is lower than that of one adsorbed O_2 molecule and one gaseous CO molecule (step A). The co-interaction of adsorbed CO molecules and adsorbed O_2 molecules directly gives rise to intermediate OCOO (via TS7, denoted as M_{LH1}) and CO_3 (via TS8, denoted as M_{LH2}), respectively. For M_{LH1}, in TS7, the distance between the carbon atom in the CO

molecule and the oxygen atom in adsorbed O_2 decreases from 2.818 to 2.290 Å, suggesting the formation of the OOCO intermediate. This step has an energy barrier of 0.72 eV, and exothermicity is found to be 0.68 eV. Unlike path M_{LH1}, M_{LH2} involves the co-interaction of adsorbed CO and adsorbed O_2 to form the CO_3 intermediate. Although the process is exothermic by 2.51 eV, it has a high energy barrier of 1.60 eV (TS8), which hinders M_{LH2} reaction channels.

From the above results, it is clear that CO oxidation on the defective $PdCl_2$ (140) surface can proceed along the E-R and L-H mechanisms because of their moderate barrier height and high exothermicity. Because of the smallest barrier involved in M_{ER1}, the CO oxidation on the surface prefers to follow an E-R mechanism, which has previously been observed for metal surfaces[52, 53], metal doped surfaces[9], and some oxide surfaces[4, 17]. The reaction activation barrier (0.54 eV) of CO oxidation in the $PdCl_2$ catalyst is low, indicating the potential high catalytic performance of the $PdCl_2$ catalyst for CO oxidation.

4. Conclusions

In summary, the detailed structural information of adsorbed CO and the chemical reaction mechanism of CO oxidation on defective $PdCl_2$ (140) surfaces has been studied within the DFT computation framework, *in situ* DRIRS, and EXAFS measurements. The defective (140) facet is identified as the active plane in $PdCl_2$ catalysts. We found that the path along M_{ER1} appears to perform the best, in which the largest barrier is only 0.54 eV and must be overcome. The reaction

channel proceeds first via a peroxo-type (OOCO) intermediate formation, second by O adsorption with the first CO_2 release, then by the second CO attraction and the second CO_2 formation, and finally by the second CO_2 desorption and restoration of the defective $PdCl_2$ (140) surface. The rate-determining step is the formation of the second CO_2 in the catalytic cycle. The $PdCl_2$ catalyst is as good as other transition metal nanostructures, the reaction activation barrier of CO oxidation is low, indicating as a potential high-performance catalyst for CO oxidation. In addition, the XPS results and the XANES and EXAFS results indicate the defective structure of $PdCl_2/\alpha$-Al_2O_3. It is hoped that the present theoretical investigations will provide experiments with instructive information on further exploring the CO oxidation on palladium-based catalysts.

Acknowledgements

This work is supported by NSFC projects (Nos. 21201165, 21171165, and 21501177) and FJPNSF projects (2013J05040 and 2015H0053). We also acknowledge the Supercomputing Centre of CNIC for providing the computer resources.

References

1. M. Haruta, *Catal. Tod.*, 1997, **36**, 153-166.
2. R. G. S. Pala, W. Tang, M. M. Sushchikh, J.-N. Park, A. J. Forman, G. Wu, A. Kleiman-Shwarsctein, J. Zhang, E. W. McFarland and H. Metiu, *J. Catal.*, 2009, **266**, 50-58.
3. Fang Wang, D. Zhang, X. Xu and Y. Ding, *J. Phys. Chem. C*, 2009, **113**, 18032-18039.
4. A. Farkas, G. C. Mellau and H. Over, *J. Phys. Chem. C*, 2009, **113**, 14341-14355.
5. Qiaohong Li, Zhangfeng Zhou, Ruiping Chen, Baozhen Sun, Luyang Qiao, Yuangen Yao and K. Wu, *Phys. Chem. Chem. Phys.*, 2015, **17**, 9126-9134.
6. S.-Y. Wang, N. Li, L.-F. Luo, W.-X. Huang, Z.-Y. Pu, Y.-J. Wang, G.-S. Hu, M.-F. Luo and J.-Q. Lu, *Appl. Catal. B: Environ.*, 2014, **144**, 325-332.
7. C. Tang, J. Sun, X. Yao, Y. Cao, L. Liu, C. Ge, F. Gao and L. Dong, *Appl. Catal. B: Environ.*, 2014, **146**, 201-212.
8. Y.-G. Wang, Y. Yoon, V.-A. Glezakou, J. Li and R. Rousseau, *J. Am. Chem. Soc.*, 2013, **135**, 10673-10683.
9. S. Lin, X. Ye, R. S. Johnson and H. Guo, *J. Phys. Chem. C*, 2013, **117**, 17319-17326.
10. J. Gustafson, R. Westerström, A. Mikkelsen, X. Torrelles, O. Balmes, N. Bovet, J. N. Andersen, C. Baddeley and E. Lundgren, *Phy. Rev. B*, 2008, **78**, 045423.
11. B. Qiao, A. Wang, X. Yang, L. F. Allard, Z. Jiang, Y. Cui, J. Liu, J. Li and T. Zhang, *Nat. Chem.*, 2011, **3**, 634-641.
12. M. Moses-DeBusk, M. Yoon, L. F. Allard, D. R. Mullins, Z. Wu, X. Yang, G. Veith, G. M. Stocks and C. K. Narula, *J Am. Chem. Soc.*, 2013, **135**, 12634-12645.
13. Y. Li, Yue Yu, J.-G. Wang, J. Song, Q. Li, M. Dong and C.-J. Liu, *Appl. Catal. B: Environ.*, 2012, **125**, 189-196.
14. X. Liu, Y. Sui, T. Duan, C. Meng and Y. Han, *Phys. Chem. Chem. Phys.*, 2014, **16**, 23584-23593.
15. X. Tang, J. Schneider, A. Dollinger, Y. Luo, A. Wörz, K. Judai, S. Abbet, Y. Kim, G. Ganteför and D. Fairbrother, *Phys. Chem. Chem. Phys.*, 2014, **16**, 6735-6742.
16. D. Vogel, C. Spiel, Y. Suchorski, A. Trinchero, R. Schlogl, H. Gronbeck and G. Rupprechter, *Angew. Chem. Int. Ed.*, 2012, **51**, 10041-10044.
17. B. Z. Sun, W. K. Chen and Y. J. Xu, *J. Chem. Phys.*, 2010, **133**, 154502.
18. J. Lin, A. Wang, B. Qiao, X. Liu, X. Yang, X. Wang, J. Liang, J. Li, J. Liu and T. Zhang, *J. Am. Chem. Soc.*, 2013, **135**, 15314-15317.
19. Z. Huang, X. Gu, Q. Cao, P. Hu, J. Hao, J. Li and X. Tang, *Angew. Chem. Int. Ed.*, 2012, **51**, 4198-4203.
20. J.-X. Liang, J. Lin, X.-F. Yang, A.-Q. Wang, B.-T. Qiao, J. Liu, T. Zhang and J. Li, *J. Phys. Chem. C*, 2014, **118**, 21945-21951.
21. E. J. Peterson, A. T. DeLaRiva, S. Lin, R. S. Johnson, H. Guo, J. T. Miller, J. Hun Kwak, C. H. Peden, B. Kiefer, L. F. Allard, F. H. Ribeiro and A. K. Datye, *Nat. Commun.*, 2014, **5**, 4885-4895.
22. Y. Yamamoto, *Catal. Surv. Asia*, 2010, **14**, 103-110.
23. B. Kalita and R. C. Deka, *J. Am. Chem. Soc.*, 2009, **131**, 13252–13254
24. W.-C. Ding, X.-K. Gu, H.-Y. Su and W.-X. Li, *J. Phys. Chem. C*, 2014, **118**, 12216-12223.
25. J. Zhang, H. Jin, M. B. Sullivan, F. C. Lim and P. Wu, *Phys. Chem. Chem. Phys*, 2009, **11**, 1441-1446.
26. S.-i. Uchiumi, K. Ataka and T. Matsuzaki, *J. Organ. Chem.*, 1999, **576**, 279-289.

27. X. Ding, X. Dong, D. Kuang, S. Wang, X. Zhao and Y. Wang, *Chem. Eng. J.*, 2014, **240**, 221-227.
28. Y. Yamamoto, T. Matsuzaki, S. Tanaka, K. Nishihira, K. Ohdan, A. Nakamura and Y. Okamoto, *J. Chem. Soc. Faraday Transactions*, 1997, **93**, 3721-3727.
29. Q. Meng, S. Wang, Y. Shen, B. Yan, Y. Wu and X. Ma, *Appl. Surf. Sci.*, 2014, **292**, 117-127.
30. B. Delley, *J. Chem. Phys.*, 1990, **92**, 508-517.
31. B. Delley, *J. Chem. Phys.* , 2000, **113**, 7756-7764.
32. J. P. Perdew and Y. Wang, *Phys. Rev. B*, 1992, **45**, 13244-13249.
33. L. Versluis and T. Ziegler, *J. Chem. Phys.*, 1988, **88**, 322-328.
34. U. von Barth and L. Hedin, *J. Phys. C: Solid State Phys.*, 1972, **5**, 1629-1642.
35. C.-S. Lee, T.-S. Hwang, Y. Wang, S.-M. Peng and C.-S. Hwang, *J. Phys. Chem.*, 1996, **100**, 2934-2941.
36. Z. G. Wang, Q. D. Zeng, Y. B. Luan, X. J. Wu, L. J. Wan, C. Wang, G. U. Lee, S. X. Yin, J. L. Yang and C. L. Bai, *J. Phys. Chem. B*, 2003, **107**, 13384-13388.
37. T. T. Lin, W.-D. Zhang, J. C. Huang and C. B. He, *J. Phys. Chem. B*, 2005, **109**, 13755-13760.
38. N. Matsuzawa, J. e. Seto and D. A. Dixon, *J. Phys. Chem. A*, 1997, **101**, 9391-9398.
39. Y. Gao, W. Peng, N. Zhao, W. Wei and Y. Sun, *J. Mol. Catal. A: Chem.*, 2011, **351**, 29-40.
40. Y. Shen, Q. Meng, S. Huang, S. Wang, J. Gong and X. Ma, *RSC Advances*, 2012, **2**, 7109-7119.
41. R. Zhang, L. Song, B. Wang and Z. Li, *J Comput. Chem.*, 2012, **33**, 1101-1110.
42. Y. Shen, Q. Meng, S. Huang, J. Gong and X. Ma, *Phys. Chem. Chem. Phys.*, 2013, **15**, 13116-13127.
43. J. Ren, W. Wang, D. Wang, Z. Zuo, J. Lin and Z. Li, *Appl. Catal. A Gen.*, 2014, **472**, 47-52.
44. Y. Shen, S. Wang, S. Huang, Z. Li and X. Ma, *Appl. Surf. Sci.*, 2014, **308**, 237-246.
45. B. Ravel and M. Newville, *J Synchrotron Rad.*, 2005, **12**, 537-541.
46. M. Newville, *J Synchrotron Rad.*, 2001, **8**, 322-324.
47. *JCPDS standard diffraction file No. 01-0228*.
48. K. Guo, H. Ye and Y. Wu, *Application of electron diffraction patterns in crystallography*, Science Press 1983.
49. S. Y. Peng, Z. N. Xu, Q. S. Chen, Y. M. Chen, J. Sun, Z. Q. Wang, M. S. Wang and G. C. Guo, *Chem. Commun.*, 2013, **49**, 5718-5720.
50. K. I. Choi and M. A. Vannice, *J Catal.*, 1991, **127**, 465-488.
51. J. Lin, B. Qiao, L. Li, H. Guan, C. Ruan, A. Wang, W. Zhang, X. Wang and T. Zhang, *J Catal.*, 2014, **319**, 142-149.
52. Z.-P. Liu, P. H. * and A. Alavi, *J. Am. Chem. Soc.*, 2002, **124**, 14770-14779.
53. B. Kalita and R. C. Deka*, *J. Am. Chem. Soc.*, 2009, **131**, 13252-13254.

Figure captions

Fig. 1. Top and side views of the perfect $PdCl_2$ (140) surface. The Pd and Cl atoms are coloured in blue and green, respectively.

Fig. 2A. (1) HRTEM image of the fresh $PdCl_2/\alpha$-Al_2O_3 catalyst; (2) XRD profiles of the $PdCl_2/\alpha$-Al_2O_3 catalyst; (3) curve fit of Pd and $PdCl_2$ 3d peaks for XPS profiles of the $PdCl_2/\alpha$-Al_2O_3 catalyst.

Fig. 2B. (1) XANES spectra; (2) k^2-Weighted Fourier transforms the Pd K-edge EXAFS spectra of the $PdCl_2/\alpha$-Al_2O_3 catalyst: (A) pure $PdCl_2$, (B) $PdCl_2/\alpha$-Al_2O_3, (C) Pd foil; (3) EXAFS data (black) and fit data (red) of the $PdCl_2/\alpha$-Al_2O_3 catalyst.

Fig. 3 Optimized stable structures of single CO (M1) and O_2 (N1-N3) molecule adsorption on the defective $PdCl_2$ (140) surface. The values in parentheses for CO and O_2 are the experimental bond lengths. The bond lengths and the adsorption energies are given in angstrom and eV, respectively. The Pd, Cl, C, and O atoms are coloured in blue, green, grey, and red, respectively. The same colour scheme is applied in Figs. 4 and 8.

Fig. 4. Optimized stable intermediates A: peroxo-type (OOCO) and B: carbonate-like (CO_3) formed by CO and O_2 co-adsorption. The values in the blue rectangle indicate Mulliken charges. The bond lengths and the adsorption energies are given in angstrom and eV, respectively.

Fig. 5. DOS of the separate components (CO, O_2, and Pd, respectively) before and after adsorption. (a) for OOCO and (b) for CO_3.

Fig. 6. IR spectra of CO and O_2 reactions on the $PdCl_2/\alpha$-Al_2O_3 catalyst at different temperatures. The *in situ* infrared measurements were taken through the gas, and the temperature reached the specified temperature after balance and after 10 min of data acquisition.

Fig. 7. Four proposed reaction pathways for CO oxidation on the defective $PdCl_2$ (140) surface. M_{ER1} (green), M_{ER2} (blue), M_{LH1} (purple), and M_{LH2} (red). The energy and bond lengths are given in eV and angstroms, respectively.

Fig. 8. Side view of the proposed reaction pathway for CO oxidation on the defective $PdCl_2$ (140) surface. See the caption of Fig. 7.